First Demonstration of Spaceborne SAR Terrain Matching Curved Imaging With LJ2-01 Satellite

Yan Wang, *Member, IEEE*, Xuan Wang, *Graduate Student Member, IEEE*, Hanwei Sun, *Member, IEEE*, Ke Chen, *Graduate Student Member, IEEE*, Qingjun Zhang, *Member, IEEE*, Qingrui Guo, *Member, IEEE*, Ziheng Liu, *Graduate Student Member, IEEE*, Yong Zhao, Heli Gao, Bingyi Li, Dehua He, Guo Zhang, *Member, IEEE*, Zegang Ding, *Senior Member, IEEE*, and Tao Zeng, *Senior Member, IEEE*

***Abstract*— The swath of the conventional spaceborne synthetic aperture radar (SAR) is parallel-to-orbit, making it inefficient to observe long curved terrain, such as coastlines, railways, and so on. Imaging long curved terrains with the terrain matching (TM) curved swath is a promising technique for efficient data acquisition. The key feature is the employment of a long curved swath matching with the orientations of the long curved terrains. This article reports the first demonstration of the spaceborne SAR TM curved imaging with the LJ2-01 satellite. A TM curved swath of 161.7 km is imaged with an azimuth resolution of 0.6 m. The main technical contributions are as follows. First, a new electrical-mechanical-combined beam control method is proposed to achieve uniform azimuth resolution. Second, a new nonuniform pulse repetition frequency (PRF) sequence is used to mitigate the data loss caused by the violent spatial variation of the slant range. Third, a new swath-adaptive subaperture time-domain imaging algorithm is proposed for efficient TM curved swath imaging. These innovations contribute to successful data acquisition and imaging of the spaceborne SAR TM curved imaging with the LJ2-01 satellite.**

***Index Terms*— Electrical-mechanical-combined beam control, LJ2-01 satellite, nonuniform pulse repetition frequency (PRF) sequence, spaceborne synthetic aperture radar (SAR), swath-adaptive subaperture time-domain imaging algorithm, terrain matching (TM) curved imaging.**

I. Introduction

THE swath of the conventional spaceborne synthetic aperture radar (SAR) is parallel to the satellite track during the observation, suffering from the incomplete coverage of the long curved terrains, as shown in Fig. 1(a) [1], [2], [3], [4], [5]. The long curved terrains are important for the spaceborne SAR observation with typical ones as coastlines [6], [7], [8], railways [9], [10], rivers [11], [12], seismic faults [13], [14], [15], [16], and so on.

The conventional solution is to use multiple parallel-to-orbit swathes to increase the overall swath width for better coverage, as shown in Fig. 1(b). The main realization methods include multipass revisit [17], [18], multisatellite networking [19], [20], [21], [22], single-pass time-division observing [23], [24], [25], [26], [27], and multichannel transmitting and receiving [28], [29], [30]. However, all of them suffer from inevitable shortcomings and, hence, are not the optimum solution, as analyzed in Table I.

Imaging a long curved terrain with a terrain matching (TM) curved swath is a promising approach for high-efficient data acquisition, as shown in Fig. 1(c) [31], [32]. The main characteristic is the 2-D beam steering that continuously tracks the orientations of the long curved terrains.

Technically, the main challenges of realizing the TM curved imaging include the following.

1) *Nonuniform Azimuth Resolution:* The azimuth resolution is mainly influenced by the target illumination time determined by the beam footprint speed. In general, the spaceborne SAR imaging requires the azimuth resolution to be uniform [33], [34]. In the conventional SAR, the uniform azimuth resolution can be easily achieved by using a fixed beam footprint speed along the rectilinear swath. However, using a fixed beam footprint speed can no longer realize a uniform azimuth resolution along a much more complex TM curved swath due to the spatially varied target illumination time.
2) *Data Loss Caused by Constant Pulse Repetition Frequency:* The core of the azimuth sampling is to find a suitable pulse repetition frequency (PRF) sequence for high-quality data acquisition, i.e., preventing the valid echoes from being overwhelmed by the transmitted pulses or polluted by the nadir returns [35], [36]. While a constant PRF sequence is enabled to achieve high-quality data acquisitions for the conventional SAR, it will inevitably induce severe data loss due to the severe

Manuscript received 31 October 2023; revised 2 June 2024; accepted 22 June 2024. Date of publication 29 July 2024; date of current version 30 August 2024. This work was supported in part by the National Natural Science Foundation of China under Grant 62331007, Grant 62271053, and Grant 61971042; and in part by Beijing Nova Program under Grant 20220484109 and Grant 20230484452. *(Corresponding author: Hanwei Sun.)*

Yan Wang, Zegang Ding, and Tao Zeng are with the Radar Research Laboratory, School of Information and Electronics, Beijing Institute of Technology, Beijing 100081, China, also with Yangtze Delta Region Academy, Beijing Institute of Technology, Jiaxing 314019, China, and also with Beijing Institute of Technology Chongqing Innovation Center, Chongqing 401331, China.

Xuan Wang, Ke Chen, Qingrui Guo, and Ziheng Liu are with the Radar Research Laboratory, School of Information and Electronics, Beijing Institute of Technology, Beijing 100081, China.

Hanwei Sun, Yong Zhao, and Bingyi Li are with Beijing Institute of Radio Measurement, Beijing 100854, China (e-mail: sunhw12@tsinghua.org.cn).

Qingjun Zhang, Heli Gao, and Dehua He are with the Remote Sensing Satellite General Department, China Academy of Space Technology, Beijing 100094, China.

Guo Zhang is with the State Key Laboratory of Information Engineering in Surveying, Mapping and Remote Sensing, Wuhan University, Wuhan 430079, China.

Digital Object Identifier 10.1109/TGRS.2024.3430833

TABLE I
SHORTCOMINGS OF THE CONVENTIONAL SPACEBORNE SAR IN OBSERVING LONG CURVED TERRAINS

No.	Implementation	Limit	
		Specific	Common
1	Multi-pass revisit	Long time	High redundancy
2	Multi-satellite networking	High cost	
3	Single-pass time-division (TOPSAR / ScanSAR)	Low azimuth resolution	
4	Multi-channel	Complex payload	

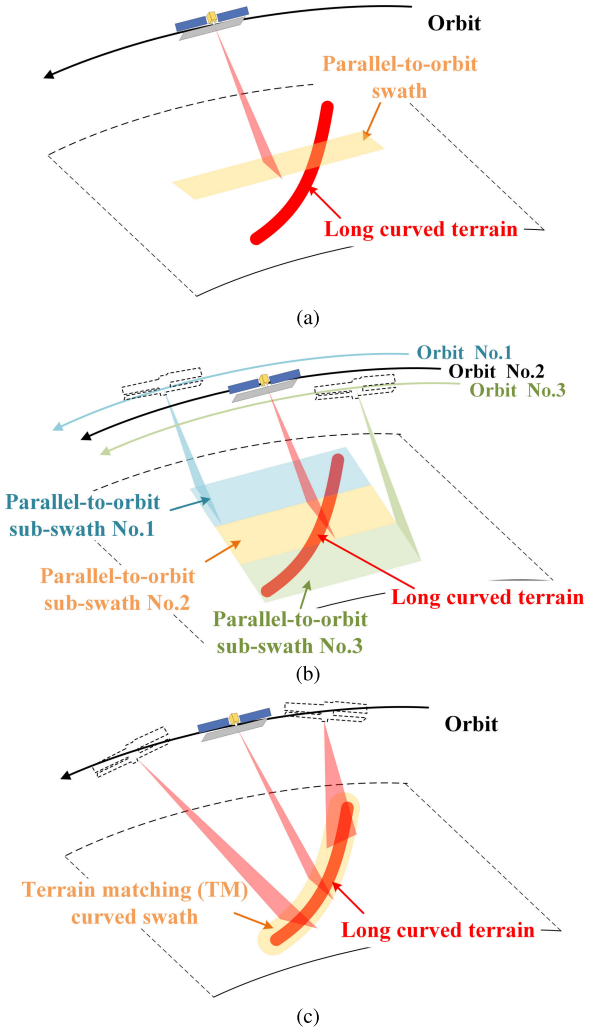

Fig. 1. Observing a long curved terrain by (a) single parallel-to-orbit swath, (b) multiple parallel-to-orbit subswathes, and (c) TM curved swath.

slant range variation caused by the 2-D continuous beam steering in the TM curved imaging.

3) *Limited Imaging Performance:* Due to the complex geometry of the TM curved imaging, the signal features of echoes turn to be much more complex, resulting in the conventional imaging algorithm having limited performance. Specifically, the conventional frequency-domain algorithms suffer from low accuracy due to the seriously spatially varied time–frequency features [37], [38]; the conventional time-domain algorithms suffer from low efficiency due to the lack of consideration for the TM curved swath feature [39], [40].

In this article, we, for the first time, realize the spaceborne SAR TM curved imaging with the Chinese LJ2-01 satellite. A TM curved swath of 161.7 km is imaged with an azimuth resolution of 0.6 m. During the whole data acquisition, the slant range along the beam center changes from 453 to 506 km, the look angle varies from 16° to 30.4°, and the squint angle varies from −7° to 7°. While, in the TM curved imaging, the data acquisition is completed in a single track of observation in 29 s, it will require up to 20 tracks of observation lasting for 40 days if using the conventional parallel-to-orbit imaging.

The detailed technical contributions include the following.

1) *Electrical-Mechanical-Combined Beam Control for Uniform Azimuth Resolution:* The beam footprint speed is spatially adjusted by the simultaneously controlling electrical and mechanical beam steering. The beam-steering discipline is to ensure that the target illumination time along the TM curved swath is consistent, resulting in a desired uniform azimuth resolution distribution. While, with a constant footprint speed, the azimuth resolution fluctuation can be up to 48.6%, a spatially varying beam footprint speed can reduce the azimuth resolution fluctuation to around 0.5% theoretically. Due to the linear azimuth beam scanning and angle quantization of LJ2-01 satellite, a spatially varying beam footprint speed can reduce the azimuth resolution fluctuation to around 6.7% in the experiment.
2) *Nonuniform PRF for Minimum Data Loss:* The azimuth sampling is implemented by using nonuniform PRF sequence for high-quality data acquisition. The way the PRF is adjusted depends on the slant range variation to ensure a minimum time overlapping among the valid echoes, the transmitted pulses, and the nadir returns. By using the nonuniform PRF sequence, the data loss ratio in the TM curved imaging data acquisition can be decreased from 49.8% to about 1%.
3) *Swath-Adaptive Subaperture Time-Domain Imaging Algorithm:* A new time-domain algorithm is proposed to adapt to the TM curved swath feature. A new grid meshing method is suggested to fit the orientation of the TM curved swath with much reduced redundancy. A new spectrum compression method is proposed to adapt to the new grid meshing manipulation. Comparing with the conventional time-domain algorithm, the new swath-adaptive subaperture time-domain imaging

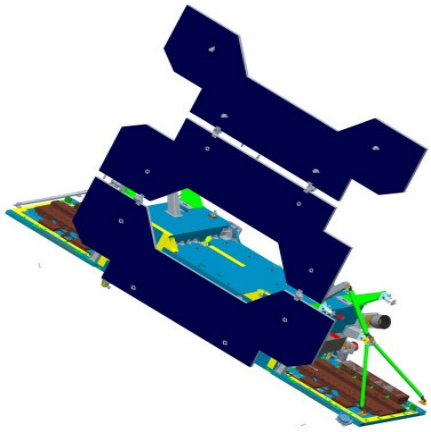

Fig. 2. LJ2-01 satellite.

algorithm can save 94% of the computation load in the experiment.

This article is organized as follows. Section II reviews the capabilities of the LJ2-01 satellite and the feasibility for realizing the TM curved imaging. Section III proposes an new beam control method to achieve a uniform azimuth resolution distribution along the TM curved swath. Section IV proposes to implement the azimuth sampling with a nonuniform PRF sequence to minimize the data loss caused by the severe slant range variation in the TM curved imaging. Section V describes a new subaperture time-domain imaging algorithm that has the adaptability to the TM curved swath feature. In Section VI, the first TM curved imaging experiment with the LJ2-01 is reported, validating the effectiveness of the proposed approaches. Section VII summarizes the study and suggests future plans.

II. Overview of the LJ2-01 Satellite

The LJ2-01 is a high-resolution Ka-band Chinese SAR satellite launched on May 21, 2023 in Fig. 2, and its working frequency is 35.75 GHz. It is equipped with a phased-array antenna with the size of 3 × 0.6 m (azimuth × range) with the highest resolution of 0.5 m.

The implementation of the spaceborne SAR TM curved imaging requires two abilities: adjustable PRF to minimize the data loss caused by the severe slant range variation and 2-D continuous beam-steering ability to track the long curved terrains.

The LJ2-01 satellite satisfies this requirement by having the following.

1) *PRF Adjustment Ability:* The LJ2-01 satellite is able to adjust the PRF up to 16 times in a single observation task, ranging from 4000 to 10 000 Hz. Each time the PRF is changed, there exists 20 ms that the echoes cannot be recorded, resulting in an inevitable echo loss.
2) *Two-Dimensional Continuous Beam-Steering Ability:* The LJ2-01 is able to realize the 2-D continuous beam steering for the long curved terrain tracking by simultaneously adjusting the beam electrically and mechanically, as shown in Fig. 3. The range beam steering is realized by mechanically rolling of the platform from 0° to 30°. The azimuth beam steering is realized by electrically steering the beam from −20° to 20°. Within the period a PRF lasts, the electrical beam steering is implemented with a constant angular speed.

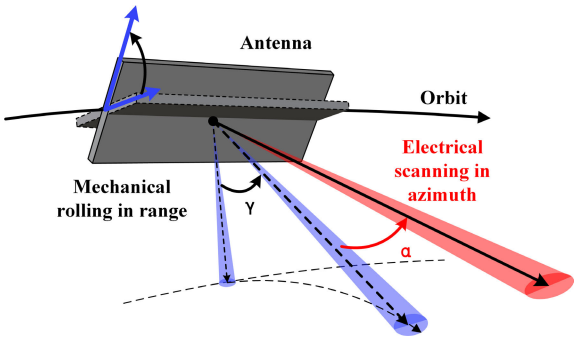

Fig. 3. Two-dimensional beam steering of the LJ2-01.

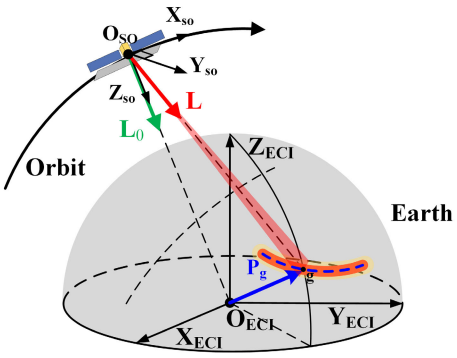

Fig. 4. Beam pointing direction in the TM curved imaging.

III. Geometry Configuration

A. Electrical-Mechanical-Combined Beam Control Model

The core of the geometry configuration is to realize a uniform azimuth resolution distribution [41], [42], [43]. It is achieved by the 2-D continuous beam steering to ensure a consistent target illumination time along the TM curved swath.

The roll angle of the LJ2-01 satellite in the idle status is zero, leading to the beam pointing to the Earth center, as shown in Figs. 3 and 4. If represented in the Earth-centered inertial (ECI) coordinate system, the unit beam vector at this status yields

$$\mathbf{L}_0 = \begin{bmatrix} -\cos\Omega\cos u + \sin\Omega\cos i\sin u \\ -\sin\Omega\cos u - \cos\Omega\cos i\sin u \\ -\sin i\sin u \end{bmatrix} \tag{1}$$

where Ω, i, and u denote the right ascension of ascending node, the orbit inclination, and the argument of latitude, respectively.

In the case a TM curved imaging task is executed, the beam vector is to be changed by the roll angle γ and the electrically beam scanning angle α as follows:

$$\mathbf{L} = \mathbf{H}(\Omega, i, u) * \mathbf{A}(\gamma, \alpha) * \mathbf{H}(\Omega, i, u)^{\mathrm{T}} * \mathbf{L}_0 \tag{2}$$

where $\mathbf{H}$ represents the transform matrix from the satellite orbit (SO) coordinate system to the ECI coordinate system in (3), as shown at the bottom of the next page. The SO coordinate system is defined as a right-hand coordinate system

established at the satellite mass center O_{SO}, as shown in Fig. 4, where the Z-axis Z_{SO} always points toward the Earth center O_{ECI} and the Y-axis Y_{SO} is perpendicular to the orbit plane. The matrix $\mathbf{A}$ represents the beam-steering behavior in the SO coordinate system as follows:

$$\mathbf{A}(\gamma,\alpha)=\begin{bmatrix}\cos(\alpha) & \sin(\alpha)\sin(\gamma) & \sin(\alpha)\cos(\gamma)\\ 0 & \cos(\gamma) & -\sin(\gamma)\\ -\sin(\alpha) & \cos(\alpha)\sin(\gamma) & \cos(\alpha)\cos(\gamma)\end{bmatrix}. \tag{4}$$

B. Beam Control Optimization for Uniform Azimuth Resolution Distribution

The azimuth resolution depends on the target beam dwell time determined by the beam-steering vector $\mathbf{L}$ in (2). The beam pointing is adjusted on the assumption that the entire TM curved swath has a uniform azimuth resolution if only N sampled positions along the TM curved swath center have consistent azimuth resolution. These N sampled positions should be close enough to each other to represent the geometrical features of the TM curved swath. Note that each of feature points is not observed discretely, but is continuously observed in a manner similar to the sliding spotlight mode. In this case, the optimization model for the beam steering yields

$$\begin{aligned}&\arg\min_{\boldsymbol{e},\boldsymbol{\varepsilon}}\left(\begin{array}{c}\sum_{k=1}^{N}\left\|\rho_{a_k}(\boldsymbol{\gamma}(\boldsymbol{e}),\boldsymbol{\alpha}(\boldsymbol{\varepsilon}))-\rho_{a0}\right\|^2\\ +\lambda\sum_{k=1}^{N}\Delta d_k(\boldsymbol{\gamma}(\boldsymbol{e}),\boldsymbol{\alpha}(\boldsymbol{\varepsilon}))\end{array}\right)\\ &\text{s.t.}\begin{cases}\boldsymbol{\gamma}=\begin{bmatrix}\gamma_0 & \gamma_1 & \cdots & \gamma_N\end{bmatrix}^{\mathrm{T}}=\mathbf{B}^{\mathrm{T}}\boldsymbol{e}\\ \boldsymbol{\alpha}=\begin{bmatrix}\alpha_0 & \alpha_1 & \cdots & \alpha_N\end{bmatrix}^{\mathrm{T}}=\mathbf{B}^{\mathrm{T}}\boldsymbol{\varepsilon}\\ |\gamma_k|\le 30,\quad |\dot{\gamma}_k|\le 1,\quad |\ddot{\gamma}_k|\le 0.04,\quad k\in[1,2,\ldots,N]\\ |\alpha_k|\le 20,\quad k\in[1,2,\ldots,N]\end{cases}\end{aligned} \tag{5}$$

where $\boldsymbol{\gamma}$ and $\boldsymbol{\alpha}$ represent the roll angle and electrical scanning angle vector at N sampled position, respectively. λ denotes the regulation factor, and Δd_k denotes the deviation between the kth sampled position and the long curved terrain. ρ_{a_k} denotes the azimuth resolution of the kth sampled position, and ρ_{a_0} denotes the expected uniform azimuth resolution, where $k\in[1,2,\ldots,N]$. The azimuth resolution mentioned here refers to the main sidelobe width of the point spread function along the iso-range line on the ground, as shown in Fig. 5, where the red dashed line denotes iso-Doppler line and the green dashed line denotes iso-range line. Therefore, the direction of the azimuth resolution varies with the squint angle and look angle.

The objective function in (5) represents simultaneously realizing that the achieved azimuth resolution is close to the required one, and that the imaging swath is along the desired curved terrain as regulated by the first and the second term.

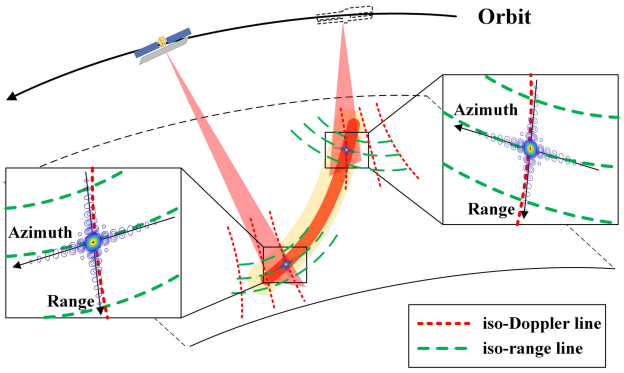

Fig. 5. Azimuth resolution direction in the TM curved imaging, where the red dashed line denotes iso-Doppler line and the green dashed line denotes iso-range line.

The physical explanations for the constraints are as follows.

1) *First and Second Constraints in (5):* $\boldsymbol{\gamma}$ and $\boldsymbol{\alpha}$ are modeled by the third-order polynomials with $\boldsymbol{e}$ and $\boldsymbol{\varepsilon}$ as the weighting factors represented as follows:

$$\begin{cases}\boldsymbol{e}=\begin{bmatrix}e_0 & e_1 & e_2 & e_3\end{bmatrix}^{\mathrm{T}}\\ \boldsymbol{\varepsilon}=\begin{bmatrix}\varepsilon_0 & \varepsilon_1 & \varepsilon_2 & \varepsilon_3\end{bmatrix}^{\mathrm{T}}.\end{cases} \tag{6}$$

The matrix $\mathbf{B}$ is the Vandermonde matrix constructed by the time basis vectors of the third-order polynomials, which can be written as $\mathbf{B}\triangleq[\mathbf{b}_1\ \ \mathbf{b}_2\ \ \cdots\ \ \mathbf{b}_N]\in\mathbb{R}^{4\times N}$, where the kth time basis vector is denoted by $\mathbf{b}_k\triangleq[t_k^0\ \ t_k^1\ \ t_k^2\ \ t_k^3]^{\mathrm{T}}\in\mathbb{R}^4$ and t_k denotes the kth sampled azimuth time.

2) *Third and Fourth Constraints in (5):* The third and fourth constraints represent the limit for the electrical and mechanical beam steering. In the LJ2-01 satellite, the maximum electrical and mechanical steering angles are 20° and 30°, respectively. $\dot{\gamma}$ and $\ddot{\gamma}$ denote the first and second derivatives of $\boldsymbol{\gamma}$ with respect to the azimuth time, indicating that the speed and acceleration of the angle steering in range should be less than the thresholds of 1 °/s and 0.04 °/s^2, respectively.

The optimization problem in (5) can be solved by using the particle swarm optimization (PSO) algorithm to achieve the weighting vector of $\boldsymbol{e}$ and $\boldsymbol{\varepsilon}$ for the 2-D continuous beam control.

IV. Azimuth Sampling

A. Necessity of Nonuniform PRF for Azimuth Sampling

The core of the azimuth sampling is to design a suitable PRF sequence to prevent the valid echoes from being either overwhelmed by the transmitted pulses or polluted by the

$$\mathbf{H}(\Omega,i,u)=\begin{bmatrix}-\cos(i)\sin(\Omega)\cos(\mu)-\cos(\Omega)\sin(\mu) & -\sin(i)\sin(\Omega) & \cos(i)\sin(\Omega)\sin(\mu)-\cos(\Omega)\cos(\mu)\\ \cos(i)\cos(\Omega)\cos(\mu)-\sin(\Omega)\sin(\mu) & \sin(i)\cos(\Omega) & -\cos(\mu)\sin(\Omega)-\cos(i)\cos(\Omega)\sin(\mu)\\ \sin(i)\cos(\mu) & -\cos(i) & -\sin(i)\sin(\mu)\end{bmatrix} \tag{3}$$

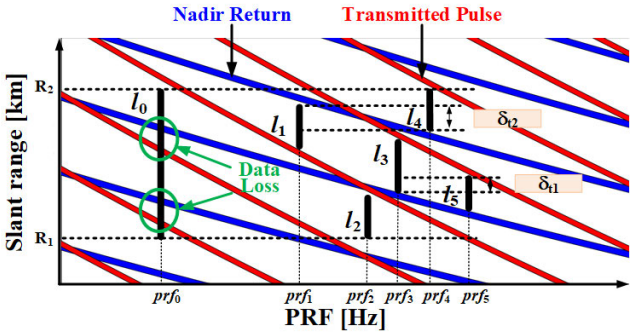

Fig. 6. Timing diagram of adopting different PRF sequences, where black solid line denotes the PRF sequence, and the red and blue zones denote the time overlaps with the transmitted pulses and the nadir returns, respectively.

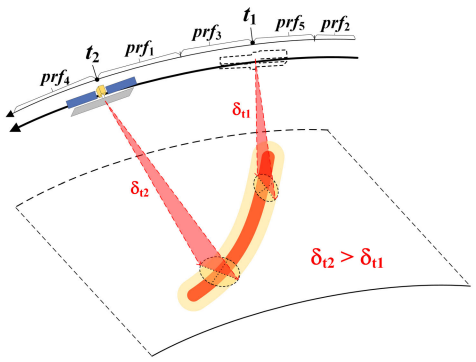

Fig. 7. Slant range variation in the TM curved imaging.

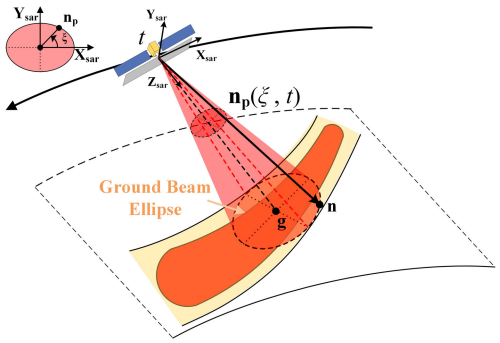

Fig. 8. Beam illumination ellipse model in the TM curved imaging.

nadir returns. A traditional constant PRF sequence is unable to achieve this in the case of the violent slant range variation in the TM curved imaging [44], [45]. Take the timing diagram in Fig. 6 as an example, where the slant range of a TM curved imaging task varies from R_1 to R_2. If a constant PRF f_0 is used for data acquisition, the problem of the transmission overwhelming and the nadir return pollution will inevitably occur as indicated by the vertical segment l_0 that overlaps with the red and blue belts.

A possible solution is to use a nonuniform PRF sequence for the azimuth sampling, i.e., replacing the long vertical segment l_0 by multiple shorter segments, such as l_1, l_2, ..., l_5 corresponding to different PRFs of prf_1, prf_2, ..., prf_5 in Fig. 6, respectively. For each of these individual PRFs, both transmission overwhelming and the nadir return pollution can be avoided [46], [47]. In a typical TM curved imaging task, the data loss caused by using a constant PRF sequence can be up to around 44%, leading to the high spikes and, hence, the degradation of integrated sidelobe ratio (ISLR) from −9.8 dB to around −1.5 dB. If using a nonuniform PRF sequence, the data loss can be reduced to only around 1%, leading to a negligible ISLR degradation from −9.8 dB to around −9.3 dB. This few data loss is caused by the PRF changes among the period of pulses transmitting and receiving, which has not been considered in the timing diagram in Fig. 6.

B. Nonuniform PRF Design

The key of designing a nonuniform PRF sequence is to ensure that at the time instant when the PRF changes, both the adjacent two PRFs are valid for the data acquisition. Take the five PRF segments in Fig. 6 as an example, where the PRF changes from prf_5 to prf_3 at time t_1 and changes from prf_1 to prf_4 at time t_2, as shown in Fig. 7. Assume that at t_1 and t_2, the maximum slant range variations, i.e., the difference between the maximum and minimum slant ranges within the beam illumination area, are δ_{t1} and δ_{t2}, respectively. In this case, prf_5 to prf_3 should have a overlapping part larger than δ_{t1}, and prf_1 to prf_4 should have a overlapping part larger than δ_{t2}. Note that δ_{t1} and δ_{t2} are different, and hence, the nonuniform PRF sequence should consider the minimum required overlapping part between the adjacent two PRFs.

Assume $\mathbf{n}_p$ as the vector pointing from the satellite antenna to an arbitrary point on the ground beam ellipse edge, as shown in Fig. 8. The instant slant range variation δ at azimuth time t, i.e., the difference between the maximum and minimum moduli of $\mathbf{n}_p$, can be represented as follows:

$$\delta(t) = \max\left(\left\|\mathbf{n}_p(\xi, t)\right\|_2\right) - \min\left(\left\|\mathbf{n}_p(\xi, t)\right\|_2\right) \tag{7}$$

where $||\cdot||_2$ denotes calculating the modulus. ξ denotes the angle parameter indicating the direction of $\mathbf{n}_p$, which rotates counterclockwise on the beam elliptic cone surface and ranges from 0° to 360°.

The calculation of the maximum and minimum modulus of $\mathbf{n}_p$ is explained in the Appendix. Therefore, the slant range variation can be obtained to instruct the minimum required overlapping part between the adjacent two PRFs.

V. Imaging Algorithm

A. Grid Meshing Along Curved Swath

Considering the limit of the conventional frequency-domain algorithm in handling the TM curved imaging echo with seriously spatial variation, the time-domain algorithm is implemented for imaging. However, the conventional time-domain algorithm, always meshing the imaging grid along the satellite track [40], will greatly lower down the imaging speed in the TM curved imaging, suffering from the plenty of redundant grids marked in green, as shown in Fig. 9(a).

To solve this problem, a new grid meshing method is proposed to implement grid meshing along the curved swath, as shown in Fig. 9(b), where the X-axis denotes the extension direction, which is reasonably selected, e.g., pointing from the start to the end of the TM curved swath. The Y-axis is perpendicular to the X-axis satisfying the right-hand rule.

To make the grid adapt to the orientation of the TM curved swath, a nonorthogonal relationship between the grids

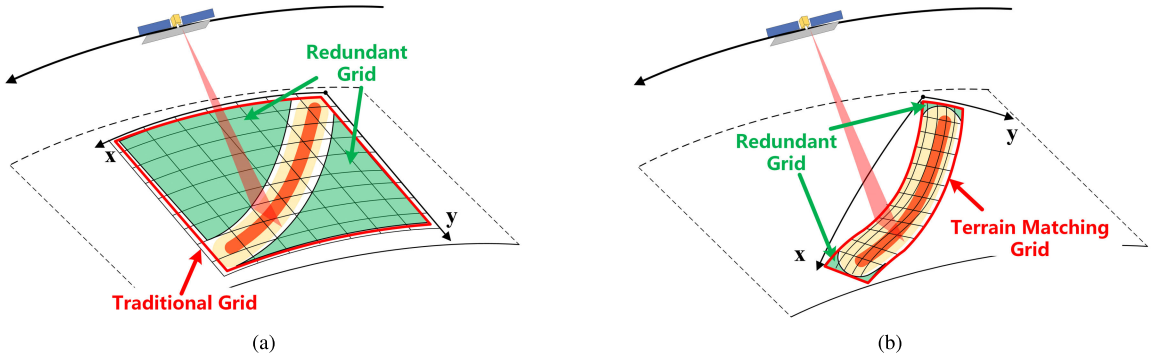

Fig. 9. Comparison of (a) conventional grid and (b) TM grid.

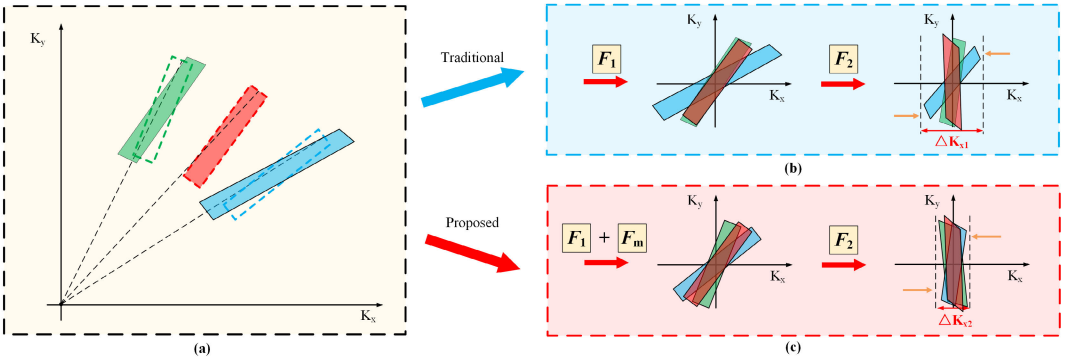

Fig. 10. Two-dimensional wavenumber spectrum variation while using the TM grid. (a) Wavenumber spectrum of three different targets, and the wavenumber spectrum processed by (b) traditional spectrum compression method and (c) proposed spectrum compression method.

is achieved by shifting the grid parallel with the Y-axis, and hence, the new grid, referred to as the TM grid, can be generated along the TM curved swath. Comparing with the conventional grid, the TM grid can achieve much less grid redundancy, contributing to a higher efficiency in the TM curved imaging.

B. Spectrum Compression With Curved Grid

The time-domain processing can be accelerated by the subaperture processing [48], [49], [50], [51]. The core of the subaperture processing is the spectrum compression that corrects the spectrum inclination and, hence, narrows the spectrum width [52]. However, comparing with the traditional grid, the nonorthogonal relationship of the TM grid results in a twisted spectrum shape, as shown in Fig. 10(a), where the 2-D wavenumber spectrum is distorted differently. In this case, if still using the traditional spectrum compression filter F_1 and F_2 in [52], the spectrum twist will cause the failure of spectrum inclination correction, resulting in an increased residual spectrum width ΔK_{x1} and reducing the imaging efficiency, as shown in Fig. 10(b).

Therefore, a new spectrum compression method is proposed with an additional spectrum distortion correcting process. It can remove the spectrum twist according to the TM curved swath to achieve the spectrum compression with a minimum spectrum width ΔK_{x2}, as shown in Fig. 10(c).

The spectrum distortion correcting filter F_m yields

$$F_m(x_i, K_y) = -K_y \times \Delta y(x_i) \tag{8}$$

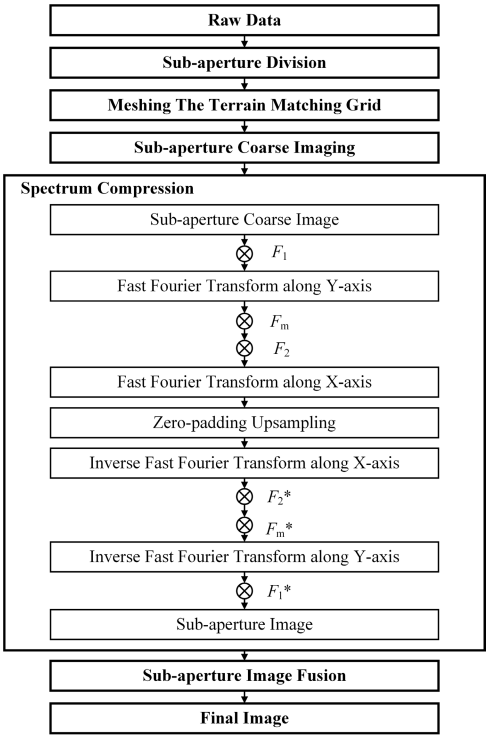

Fig. 11. Flowchart of the proposed time-domain algorithm.

where $\Delta y(x_i)$ denotes the shift of grid along the Y-axis at the different grid coordinates x_i corresponding to the orientation of the TM curved swath. By suppressing the spectrum into a minimum width, an efficient upsampling process can be

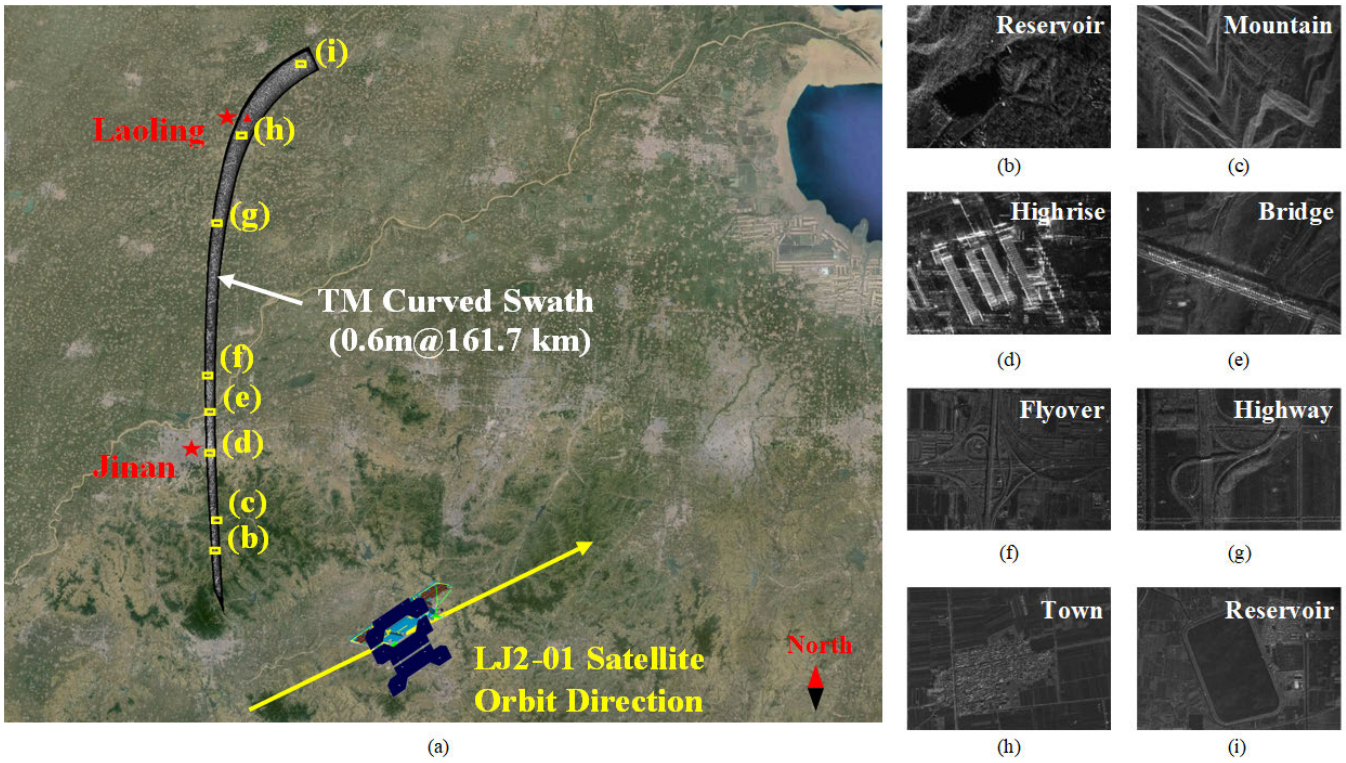

Fig. 12. TM curved swath distribution and the detail target images of the experiment.

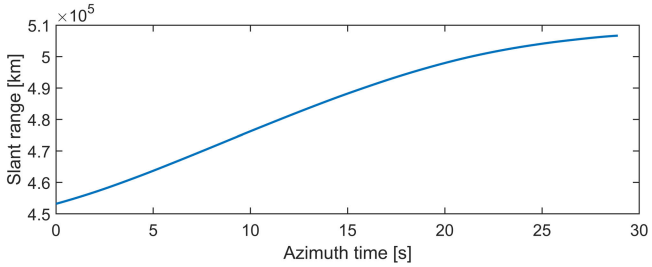

Fig. 13. Slant range variation with respect to the azimuth time.

conducted by zero padding in the 2-D wavenumber domain to achieve a high efficiency in the TM curved imaging. The flowchart of the time-domain algorithm with the proposed method is shown in Fig. 11, where $*$ denotes the conjugation processing.

VI. Experiment With LJ2-01

A. Overview

A long curved terrain of 161.7 km from Jinan to Laoling in China has been chosen as the test site for the first TM curved imaging demonstration, as shown in Fig. 12, where the SO direction is marked as a yellow arrow. The detailed images of the typical targets are displayed on the bottom, containing reservoir, mountain, flyover, town, and bridge on the Yellow River. The total imaging time is 29 s, and the slant range between the long curved terrain and the SO varies from 453 to 506 km, as shown in Fig. 13.

B. Beam Control

Based on the proposed beam control optimization method mentioned in Section III, the 2-D continuous beam steering

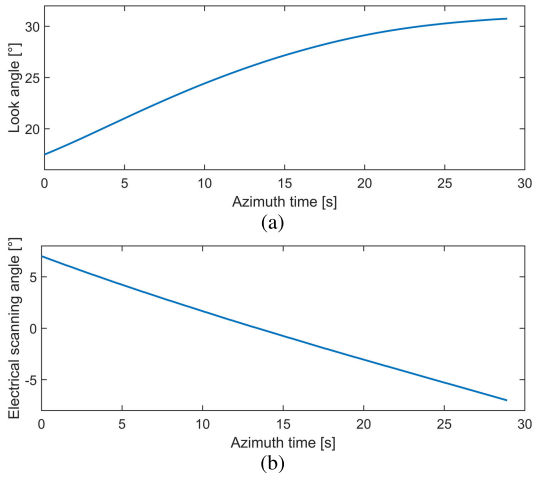

Fig. 14. Variation of (a) look angle and (b) electrical scanning angle with respect to the azimuth time.

is achieved, as shown in Fig. 14. The look angle varies from 17° to 30.7°, and the electrical scanning angle varies from −7° to 7°, as shown in Fig. 14(a) and (b), respectively. A uniform azimuth resolution distribution along the TM curved swath is realized by the spatially varying beam foot speed, as shown in Fig. 15, where the designed azimuth resolution fluctuation marked by blue is about 0.5%. The real value of azimuth resolution fluctuation marked by red is around 6.7% in the experiment. There are a deviation between the designed value and the real value of azimuth resolution fluctuation due to the limitation of the LJ2-01 satellite. Specifically, the electrical beam steering can only be implemented with a constant angular speed, and the electrical beam-steering

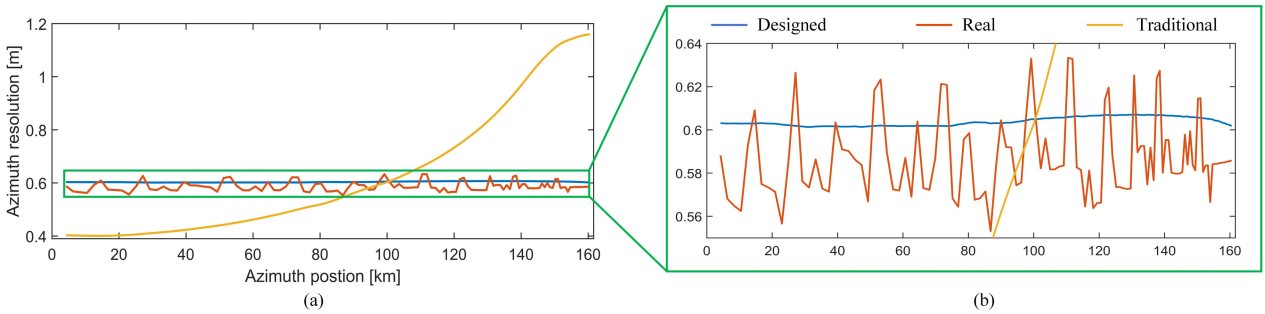

(a) (b)

Fig. 15. Azimuth resolution fluctuation along the TM curved swath by using a spatially varying beam footprint speed marked by orange curve and by using a constant beam footprint speed marked by blue curve. (a) Overall view. (b) Locally enlarged view.

angle should be quantified within a minimum quantization interval of 0.01°, as shown in Fig. 14. If using a constant beam footprint speed, the azimuth resolution fluctuation in the experimental terrain can be up to 48.6%, as shown by the yellow curve in Fig. 15.

The number of feature points N is chosen as 117 based on common sense, which can satisfy the needs of the optimization and will not bring too much computational burden. In the case of observing the test site with multiple parallel-to-orbit subswathes, 20 swathes with width of 7.9 km will be used, while the overlapping part between adjacent subswathes is 10%, and the coverage of total subswathes is 1.33×10^3 km^2. Compared with multiple parallel-to-orbit subswathes, the coverage of the TM curved swath is only 5.64×10^2 km^2, which reduces the data redundancy by 42%.

C. PRF

A nonuniform PRF sequence is achieved with 15 PRF segments $l_1, l_2, \ldots, l_{15}$, as shown in Fig. 16. The corresponding timing diagram is shown in Fig. 16(a), where the PRF varies from 6541 to 8740 Hz and the adjacent PRF segments have the overlapping part referring to the instant slant range variation in Fig. 16(c). The nonuniform PRF sequence is shown in Fig. 16(b). Take the five time instants between the adjacent PRF changes (l_2, l_3), (l_4, l_5), (l_8, l_9), (l_{11}, l_{12}), and (l_{14}, l_{15}) for example. The instant slant range variations corresponding to these five time instants are 2.08, 2.63, 3.17, 3.53, and 3.76 km, as shown in Fig. 16(c). To ensure the data to be received completely, the overlapping parts at these five time instants are designed as 2.18, 2.69, 3.26, 3.60, and 3.83 km, which are larger than the corresponding instant slant range variation.

Based on the nonuniform PRF sequence, a high-quality data acquisition is achieved, as shown in Fig. 17, where the echo distribution before and after compensating the receiving delay is shown in Fig. 17(a) and (b), respectively. A simulation is conducted to verify the data acquisition improvement of the nonuniform PRF sequence in the experiment. The expected echo distribution of using the nonuniform PRF sequence and a constant PRF sequence of 7000 Hz is shown in Fig. 18(a) and (b), respectively. The red zones denote the transmitted pulses, the yellow zones denote the nadir returns, and the orange zones are used to fill the image gaps caused by the nonuniform PRF sequence. The polluted part of echo is marked by the green dashed line. The expected echo distribution of the nonuniform PRF sequence is consistent with the real echo distribution in Fig. 17, where the data loss

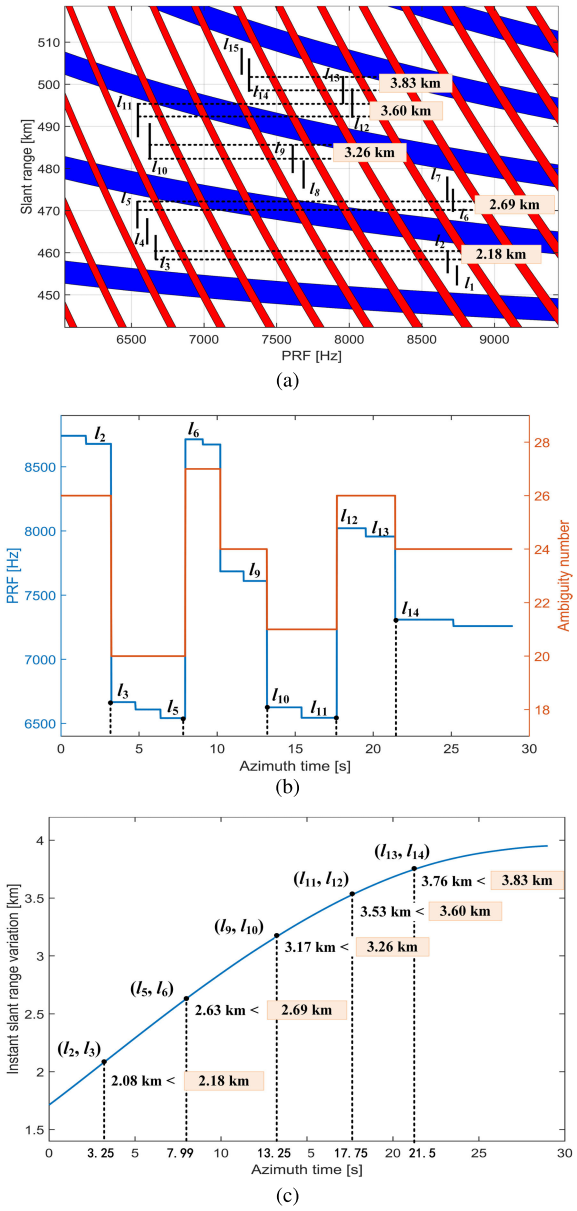

(a) (b) (c)

Fig. 16. Azimuth sampling in the experiment with (a) PRF timing diagram, (b) nonuniform PRF and the ambiguity number sequence, and (c) instant slant range variation.

ratio is only about 1%. The echo distribution of using the constant PRF sequence indicates that a large part of echo will be blocked by the transmitted pulses and the nadir returns,

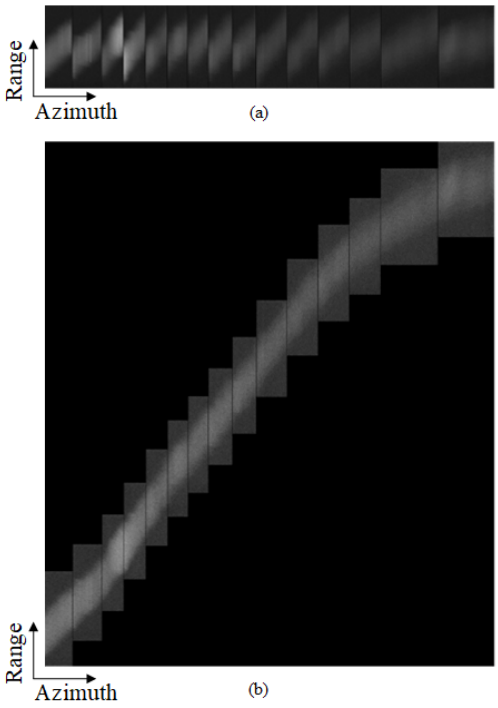

Fig. 17. Distribution of (a) original echo in the experiment and (b) echo after slant range alignment.

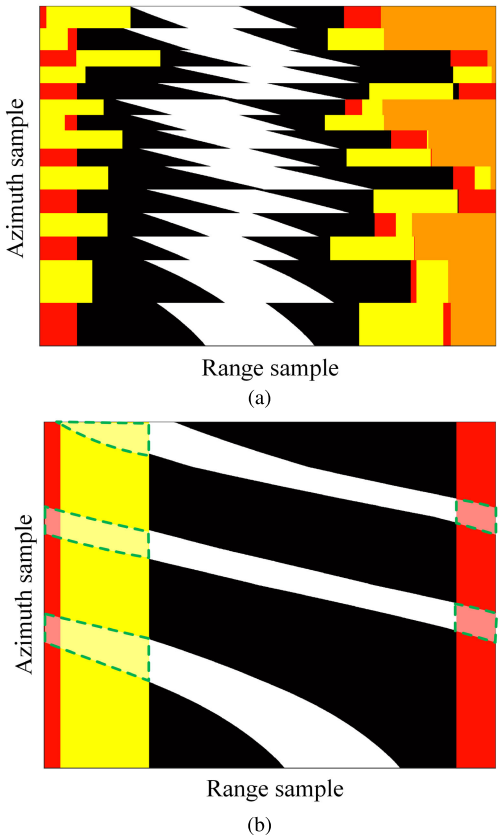

Fig. 18. Expected echo distribution in the receiving window of using (a) nonuniform PRF sequence and (b) uniform PRF sequence. The red and yellow zones denote the distribution of the transmitted pulses and the nadir returns, respectively. The orange zone is used to fill the image gaps caused by the nonuniform PRF sequence. The polluted part of echo is marked by the green dashed line.

as shown in Fig. 18(b), where the data loss ratio will reach up to 49.8%.

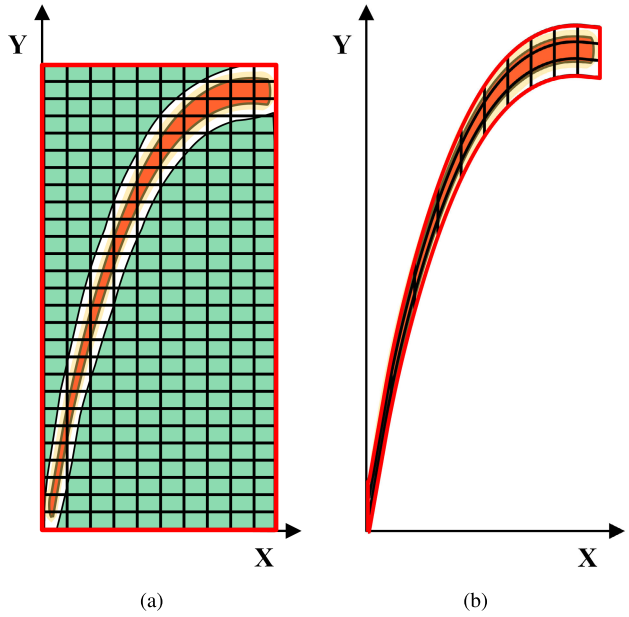

Fig. 19. Grid meshing of (a) traditional and (b) proposed method.

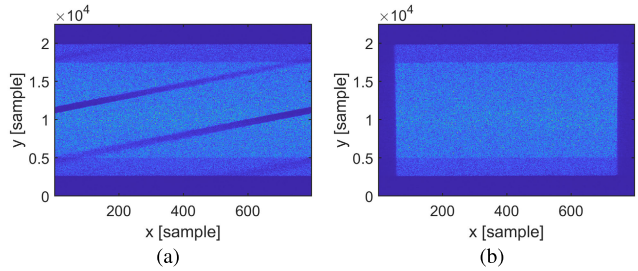

Fig. 20. Two-dimensional wavenumber of the 280th subaperture spectrum compression result processed by (a) traditional spectrum compression method in [52] and (b) proposed spectrum compression method while using TM grid.

D. Imaging

Due to the look angle variation, the TM curved swath width increases from 1.8 to 8.2 km along the long curved terrain, and the orientation of the TM curved swath has a large angle with SO direction, resulting in a increased complexity of imaging. In the case of setting traditional grid with 0.4-m interval in two dimensions, the traditional grid requires 9.14×10^{10} points to cover the whole scene, suffering from a huge redundancy marked in green, as shown in Fig. 19(a). The TM grids are meshed along the long curved terrain with only 5.28×10^{9} points, contributing to a reduced grid points by 17 times, as shown in Fig. 19(b).

The echo is divided into 338 subapertures during the imaging process. Two-dimensional wavenumber spectrum comparison at the 280th subaperture between the traditional and proposed spectrum compression methods is shown in Fig. 20. If the original spectrum is processed by the traditional spectrum compression method, the spectrum will be aliased due to the spectrum distortion, and hence, the spectrum inclination correction will fail, as shown in Fig. 20(a). If the original spectrum is processed by the proposed spectrum compression method, the spectrum distortion can be eliminated, and the spectrum inclination can be corrected completely, as shown in Fig. 20(b), ensuring the upsampling

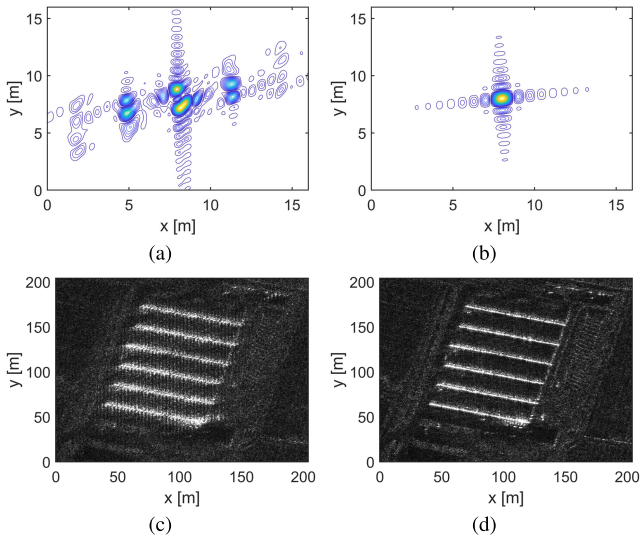

Fig. 21. Point simulation result processed by (a) traditional spectrum compression method in [52] and (b) proposed spectrum compression method with the TM grid. Local imaging result of real data in the experiment processed by (c) traditional and (d) proposed spectrum compression method.

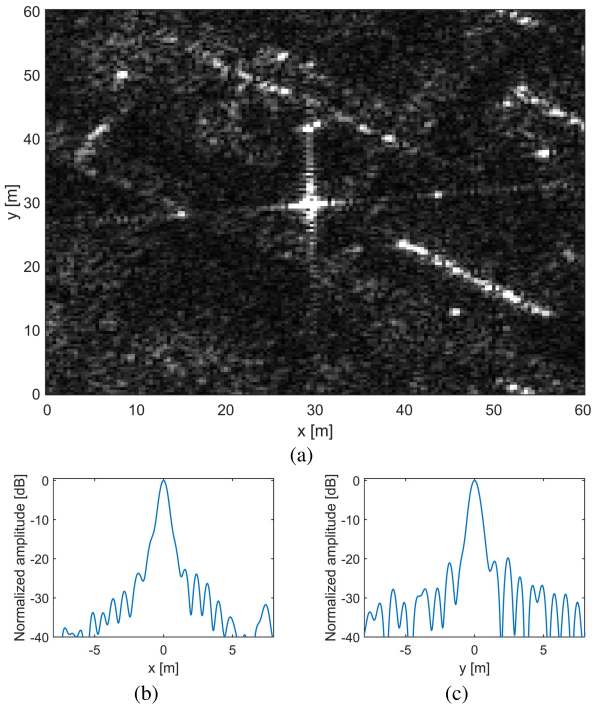

Fig. 22. Evaluation of the strong-scattered target with (a) SAR image, (b) sidelobe profile of the target along the X-axis, and (c) sidelobe profile of the target along the Y-axis.

process to perform successfully. Point simulation is performed under the same condition, as shown in Fig. 21(a) and (b). If using the traditional spectrum compression method, the point imaging result will have obvious additional grating sidelobe, as shown in Fig. 20(a), while the imaging result of the point simulation processed by the proposed spectrum compression method is well focused, as shown in Fig. 21(b). The local imaging result comparison of the 280th subaperture is shown in Fig. 21(c) and (d). If using the traditional spectrum compression method, the spectrum aliasing leads to a decrease in image quality, as shown in Fig. 21(c). If using the proposed spectrum compression method, the spectrum will not alias, and hence, the image quality keeps well, as shown in Fig. 21(d).

TABLE II
EVALUATION OF THE STRONG-SCATTERED TARGET

Parameter		Theoritical	Measured
Resolution	Azimuth	0.62 m	0.62 m
	Range	0.65 m	0.65 m
PSLR	Azimuth	-13.26 dB	-22.74 dB
	Range	-13.26 dB	-14.56 dB
ISLR	Azimuth	-9.8 dB	-11.52 dB
	Range	-9.8 dB	-11.84 dB

In the case of using the conventional time-domain algorithm in [52] and meshing the traditional grid along the satellite track, as shown in Fig. 19(a), the computation load requires 2.06×10^6 GFLOPS. In the case of using the proposed time-domain algorithm and meshing the TM grid along the TM curved swath, as shown in Fig. 19(b), the computation load only requires 1.18×10^5 GFLOPS, which contributes to a reduced computation of 16 times.

A strong-scattered target marked as a red triangle in Fig. 12 is evaluated without windowing, as shown in Fig. 22(a), and the sidelobe profile along the X- and Y-axes is represented in Fig. 22(b) and (c), respectively. As summarized in Table II, the 2-D evaluated resolutions are consistent with the designed ones, i.e., 0.62 m in azimuth and 0.65 m in range. The peak sidelobe-level ratio (PSLR) in azimuth and range is -22.74 and -14.56 dB, respectively. The ISLR in azimuth and range is -11.52 and -11.84 dB, respectively.

VII. CONCLUSION

In this article, we, for the first time, demonstrate the feasibility and advantage of the spaceborne SAR TM curved imaging with the Chinese LJ2-01 satellite. A TM curved swath of 161.7 km is imaged with an azimuth resolution of 0.6 m. In the aspect of data acquisition, a new electrical-mechanical-combined beam control method is proposed for the TM curved swath imaging with uniform azimuth resolution distribution; a new nonuniform PRF sequence is used to minimize the data loss caused by the severe slant range variation. In the aspect of imaging, a new subaperture time-domain imaging algorithm is proposed for efficient TM curved swath imaging benefiting from the adaptability to the TM curved swath feature.

In the experiment, the slant range between the long curved terrain and the SO varies from 453 to 506 km. By using the proposed method, the azimuth resolution fluctuation along the swath can be theoretically decreased from 48.6% to 0.5%. Due to the linear azimuth beam scanning and angle quantization of LJ2-01 satellite, the azimuth resolution fluctuation achieved in the experiment is around 6.7%. The data loss ratio can be decreased from 49.8% to about 1% in the experiment. The computation load of imaging can be reduced 16 times

comparing with the case of using the conventional time-domain algorithm in [52] with the traditional grid meshed along the satellite track. Considering the limits of the beam steering and the PRF adjustment of the LJ2-01 satellite, the TM curved swath in the experiment is somewhat flat. Further study will focus on realizing more complex spaceborne SAR TM curved imaging with the more flexible beam scanning capability rather than linear electrical scanning within a PRF segment.

APPENDIX
DERIVATION OF $\mathbf{n}_p$ IN (7)

Assume that the coordinate of $\mathbf{n}_p$ in the SAR antenna coordinate system is $\mathbf{n}_p = [x_p \quad y_p \quad z_p]^{\mathrm{T}}$. As pointing to an arbitrary point on the ground beam ellipse edge, as shown in Fig. 8, $\mathbf{n}_p$ is located on the beam illumination conical surface with the SAR antenna as the vertex, and this elliptical cone constraint can be represented as follows:

$$\frac{{x_p}^2}{\tan\left(\frac{\varphi_a}{2}\right)^2} + \frac{{y_p}^2}{\tan\left(\frac{\varphi_r}{2}\right)^2} = {z_p}^2 \tag{A1}$$

where φ_a and φ_r denote the 3-dB beamwidth in azimuth and range, respectively.

To describe the position of $\mathbf{n}_p$ on the elliptical cone more intuitively, ξ is introduced as the rotating angle of $\mathbf{n}_p$ from the X-axis $\mathbf{X}_{\mathrm{sar}}$ in the SAR antenna coordinate system, as shown in Fig. 8, and hence, x_p and y_p can be represented as follows:

$$\begin{cases} x_p = z_p \tan\left(\dfrac{\varphi_a}{2}\right)\cos\xi \\ y_p = z_p \tan\left(\dfrac{\varphi_r}{2}\right)\sin\xi. \end{cases} \tag{A2}$$

The ground beam ellipse edge can be approximated as the intersecting line of the beam illumination conical surface and the ground plane passing though the ground beam center point g, as shown in Fig. 8. Assume that $\mathbf{P}_g$ is the ground beam center vector, which is pointing from the Earth center to g, as shown in Fig. 4, and its coordinate is assumed as $\mathbf{P}_g = [x_g \quad y_g \quad z_g]^{\mathrm{T}}$ in the SAR antenna coordinate system. The ground plane is perpendicular to $\mathbf{P}_g$, and this plane constraint can be represented as follows:

$$x_g x_p + y_g y_p + z_g\left(z_p - R_c\right) = 0 \tag{A3}$$

where R_c denotes the slant range between the SAR antenna and g.

By substituting (A2) into (A3), the coordinates of $\mathbf{n}_p$ can be represented as follows:

$$\begin{cases} x_p = \dfrac{\tan\left(\frac{\varphi_a}{2}\right)\cos\xi z_g R_c}{z_g + x_g \tan\left(\frac{\varphi_a}{2}\right)\cos\xi + y_g \tan\left(\frac{\varphi_r}{2}\right)\sin\xi} \\ y_p = \dfrac{\tan\left(\frac{\varphi_r}{2}\right)\sin\xi z_g R_c}{z_g + x_g \tan\left(\frac{\varphi_a}{2}\right)\cos\xi + y_g \tan\left(\frac{\varphi_r}{2}\right)\sin\xi} \\ z_p = \dfrac{z_g R_c}{z_g + x_g \tan\left(\frac{\varphi_a}{2}\right)\cos\xi + y_g \tan\left(\frac{\varphi_r}{2}\right)\sin\xi}. \end{cases} \tag{A4}$$

By traversing ξ from 0° to 360° in (A4), the coordinate of $\mathbf{n}_p$ at each azimuth time instant can be obtained, and hence, the instant slant range variation along the TM curved swath can be indicated by the modulus of $\mathbf{n}_p$.

REFERENCES

[1] F. H. W. Ian G. Cumming, *Digital Processing of Synthetic Aperture Radar Data: Algorithms and Implementation*. Norwood, MA, USA: Artech House, 2005.

[2] J. C. Curlander, *Synthetic Aperture Radar: Systems and Signal Processing*. Hoboken, NJ, USA: Wiley, 1991.

[3] W. G. Carrara, *Spotlight Synthetic Aperture Radar: Signal Processing Algorithms*. Norwood, MA, USA: Artech House, 1995.

[4] M. A. Richards, *Fundamentals of Radar Signal Processing*. New York, NY, USA: McGraw-Hill, 2014.

[5] H. Rahman, *Fundamental Principles of Radar*. Boca Raton, FL, USA: CRC Press, 2019.

[6] X. Wu, C. Liu, and G. Wu, "Spatial-temporal analysis and stability investigation of coastline changes: A case study in Shenzhen, China," *IEEE J. Sel. Topics Appl. Earth Observ. Remote Sens.*, vol. 11, no. 1, pp. 45–56, Jan. 2018.

[7] M. A. Iqbal, A. Anghel, and M. Datcu, "Coastline extraction from SAR data using Doppler centroid images," *IEEE Geosci. Remote Sens. Lett.*, vol. 19, pp. 1–5, 2022.

[8] W. M. Moon, G. Staples, D. Kim, S.-E. Park, and K.-A. Park, "RADARSAT-2 and coastal applications: Surface wind, waterline, and intertidal flat roughness," *Proc. IEEE*, vol. 98, no. 5, pp. 800–815, May 2010.

[9] X. Shi, L. Jiang, H. Jiang, X. Wang, and J. Xu, "Geohazards analysis of the Litang–Batang section of Sichuan–Tibet railway using SAR interferometry," *IEEE J. Sel. Topics Appl. Earth Observ. Remote Sens.*, vol. 14, pp. 11998–12006, 2021.

[10] Y. Wang et al., "Using TerraSAR X-band and Sentinel-1 C-band SAR interferometry for deformation along Beijing-Tianjin intercity railway analysis," *IEEE J. Sel. Topics Appl. Earth Observ. Remote Sens.*, vol. 14, pp. 4832–4841, 2021.

[11] R. T. Palomaki and E. A. Sproles, "Quantifying the effect of river ice surface roughness on Sentinel-1 SAR backscatter," *Remote Sens.*, vol. 14, no. 22, p. 5644, Nov. 2022.

[12] G. Boni et al., "A prototype system for flood monitoring based on flood forecast combined with COSMO-SkyMed and Sentinel-1 data," *IEEE J. Sel. Topics Appl. Earth Observ. Remote Sens.*, vol. 9, no. 6, pp. 2794–2805, Jun. 2016.

[13] E. J. Fielding et al., "Imaging complex fault slip of large earthquakes with Sentinel-1 and ALOS-2 SAR analysis and other geodetic and seismic data," in *Proc. IEEE Int. Geosci. Remote Sens. Symp. (IGARSS)*, Jul. 2021, pp. 881–883.

[14] S. Cho, H. Xiu, and M. Matsuoka, "Backscattering characteristics of SAR images in damaged buildings due to the 2016 Kumamoto earthquake," *Remote Sens.*, vol. 15, no. 8, p. 2181, Apr. 2023.

[15] S.-W. Chen, X.-S. Wang, and M. Sato, "Urban damage level mapping based on scattering mechanism investigation using fully polarimetric SAR data for the 3.11 East Japan earthquake," *IEEE Trans. Geosci. Remote Sens.*, vol. 54, no. 12, pp. 6919–6929, Dec. 2016.

[16] M. Chini et al., "The may 12, 2008, (Mw 7.9) Sichuan earthquake (China): Multiframe ALOS-PALSAR DInSAR analysis of coseismic deformation," *IEEE Geosci. Remote Sens. Lett.*, vol. 7, no. 2, pp. 266–270, Apr. 2010.

[17] C. Hu, B. Zhang, X. Dong, Y. Li, and C. Cui, "Optimal data acquisition in multi-pass geosynchronous SAR tomography," *J. Eng.*, vol. 2019, no. 20, pp. 6359–6363, 2019.

[18] C. A. Brunori and F. Murgia, "Spatiotemporal evolution of ground subsidence and extensional basin bedrock organization: An application of multitemporal multi-satellite SAR interferometry," *Geosciences*, vol. 13, no. 4, p. 105, Apr. 2023.

[19] X. Dong, Y. Sui, Y. Li, Z. Chen, and C. Hu, "Repeat ground track SAR constellation design using revisit time image extrapolation and lookup-table-based optimization," *IEEE Trans. Geosci. Remote Sens.*, vol. 61, 2023, Art. no. 5214313.

[20] M. Badger, A. Fujita, K. Orzel, D. Hatfield, and M. Kelly, "Wind retrieval from constellations of small SAR satellites: Potential for offshore wind resource assessment," *Energies*, vol. 16, no. 9, p. 3819, Apr. 2023.

[21] D. Castelletti et al., "Capella space VHR SAR constellation: Advanced tasking patterns and future capabilities," in *Proc. IEEE Int. Geosci. Remote Sens. Symp.*, Jul. 2022, pp. 4137–4140.

[22] V. Ignatenko, P. Laurila, A. Radius, L. Lamentowski, O. Antropov, and D. Muff, "ICEYE microsatellite SAR constellation status update: Evaluation of first commercial imaging modes," in *Proc. IEEE Int. Geosci. Remote Sens. Symp.*, Sep. 2020, pp. 3581–3584.

[23] F. De Zan and A. Monti Guarnieri, "TOPSAR: Terrain observation by progressive scans," *IEEE Trans. Geosci. Remote Sens.*, vol. 44, no. 9, pp. 2352–2360, Sep. 2006.

[24] W. Xu, Y. Deng, F. Feng, Y. Liu, and G. Li, "TOPS mode raw data generation from wide-beam SAR imaging modes," *IEEE Geosci. Remote Sens. Lett.*, vol. 9, no. 4, pp. 720–724, Jul. 2012.

[25] A. Meta, J. Mittermayer, P. Prats, R. Scheiber, and U. Steinbrecher, "TOPS imaging with TerraSAR-X: Mode design and performance analysis," *IEEE Trans. Geosci. Remote Sens.*, vol. 48, no. 2, pp. 759–769, Feb. 2010.

[26] J. Holzner and R. Bamler, "Burst-mode and ScanSAR interferometry," *IEEE Trans. Geosci. Remote Sens.*, vol. 40, no. 9, pp. 1917–1934, Sep. 2002.

[27] A. Guarnieri and C. Prati, "ScanSAR focusing and interferometry," *IEEE Trans. Geosci. Remote Sens.*, vol. 34, no. 4, pp. 1029–1038, Jul. 1996.

[28] S. Chiu, "Performance analysis of RADARSAT-2 multi-channel MODEX modes," in *Proc. Eur. Microw. Conf.*, Oct. 2007, pp. 170–173.

[29] W. Xu, J. Hu, P. Huang, W. Tan, and Y. Dong, "Processing of multichannel sliding spotlight SAR data with large pulse bandwidth and azimuth steering angle," *IEEE Trans. Geosci. Remote Sens.*, vol. 60, 2022, Art. no. 5202414.

[30] G. Krieger, N. Gebert, M. Younis, F. Bordoni, A. Patyuchenko, and A. Moreira, "Advanced concepts for ultra-wide-swath SAR imaging," in *Proc. 7th Eur. Conf. Synth. Aperture Radar*, Jun. 2008, pp. 1–4.

[31] Y. Wang, Z. Li, Z. Ding, and T. Zeng, "Spaceborne large-squint terrain-matching synthetic aperture radar: Concept and technology," in *Proc. 6th Asia–Pacific Conf. Synth. Aperture Radar (APSAR)*, Nov. 2019, pp. 1–6.

[32] Y. Wang, J.-W. Li, and J. Yang, "Wide nonlinear chirp scaling algorithm for spaceborne stripmap range sweep SAR imaging," *IEEE Trans. Geosci. Remote Sens.*, vol. 55, no. 12, pp. 6922–6936, Dec. 2017.

[33] Z. Wu, L. Huang, D. Hu, and C. Ding, "Ground resolution analysis based on gradient method in geosynchronous SAR," in *Proc. IEEE Int. Conf. Signal Process., Commun. Comput. (ICSPCC)*, Aug. 2013, pp. 1–4.

[34] C. Hu, T. Zeng, Y. Zhu, and Z. Ding, "The accurate resolution analysis in geosynchronous SAR," in *Proc. 8th Eur. Conf. Synth. Aperture Radar*, Jun. 2010, pp. 1–4.

[35] Y. Wang, J. Yang, and J. Li, "Data acquisition for a novel spaceborne azimuth-range sweep synthetic aperture radar," in *Proc. IEEE Int. Geosci. Remote Sens. Symp. (IGARSS)*, Jul. 2017, pp. 6004–6007.

[36] Z.-X. Zhou, Y. Deng, W. Wang, X. Jia, and R. Wang, "Analysis of varying-PRI spotlight SAR data," *IEEE Trans. Geosci. Remote Sens.*, vol. 60, 2022, Art. no. 5221020.

[37] P. Prats, R. Scheiber, J. Mittermayer, A. Meta, and A. Moreira, "Processing of sliding spotlight and TOPS SAR data using baseband azimuth scaling," *IEEE Trans. Geosci. Remote Sens.*, vol. 48, no. 2, pp. 770–780, Feb. 2010.

[38] R. Lanari, M. Tesauro, E. Sansosti, and G. Fornaro, "Spotlight SAR data focusing based on a two-step processing approach," *IEEE Trans. Geosci. Remote Sens.*, vol. 39, no. 9, pp. 1993–2004, Sep. 2001.

[39] A. F. Yegulalp, "Fast backprojection algorithm for synthetic aperture radar," in *Proc. IEEE Radar Conf. Radar Into Next Millennium*, Apr. 1999, pp. 60–65.

[40] L. Ulander, H. Hellsten, and G. Stenstrom, "Synthetic-aperture radar processing using fast factorized back-projection," *IEEE Trans. Aerosp. Electron. Syst.*, vol. 39, no. 3, pp. 760–776, Jul. 2003.

[41] Q. Zhang, W. Yin, Z. Ding, T. Zeng, and T. Long, "An optimal resolution steering method for geosynchronous orbit SAR," *IEEE Geosci. Remote Sens. Lett.*, vol. 11, no. 10, pp. 1732–1736, Oct. 2014.

[42] Z. Ding, W. Yin, T. Zeng, and T. Long, "Radar parameter design for geosynchronous SAR in squint mode and elliptical orbit," *IEEE J. Sel. Topics Appl. Earth Observ. Remote Sens.*, vol. 9, no. 6, pp. 2720–2732, Jun. 2016.

[43] T. Zeng, W. Yin, Z. Ding, and T. Long, "Motion and Doppler characteristics analysis based on circular motion model in geosynchronous SAR," *IEEE J. Sel. Topics Appl. Earth Observ. Remote Sens.*, vol. 9, no. 3, pp. 1132–1142, Mar. 2016.

[44] Z. Men, P. Wang, C. Li, J. Chen, W. Liu, and Y. Fang, "High-temporal-resolution high-spatial-resolution spaceborne SAR based on continuously varying PRF," *Sensors*, vol. 17, no. 8, p. 1700, Jul. 2017.

[45] W. Yin, Z. Ding, S. Yang, Y. Li, T. Zeng, and T. Long, "A continuous PRI variation method for geosynchronous SAR with elliptical orbit," in *Proc. IEEE Int. Geosci. Remote Sens. Symp. (IGARSS)*, Jul. 2015, pp. 4582–4585.

[46] Y. Wang, J. Li, J. Yang, and B. Sun, "A novel spaceborne sliding spotlight range sweep synthetic aperture radar: System and imaging," *Remote Sens.*, vol. 9, no. 8, p. 783, Jul. 2017.

[47] Y. Wang, Z. Ding, P. Xu, K. Chen, T. Zeng, and T. Long, "Strip layering diagram-based optimum continuously varying pulse interval sequence design for extremely high-resolution spaceborne sliding spotlight SAR," *IEEE Trans. Geosci. Remote Sens.*, vol. 59, no. 8, pp. 6751–6770, Aug. 2021.

[48] L. Zhang, H. Li, Z. Qiao, M. Xing, and Z. Bao, "Integrating autofocus techniques with fast factorized back-projection for high-resolution spotlight SAR imaging," *IEEE Geosci. Remote Sens. Lett.*, vol. 10, no. 6, pp. 1394–1398, Nov. 2013.

[49] L. Zhang, H. Li, Z. Qiao, and Z. Xu, "A fast BP algorithm with wavenumber spectrum fusion for high-resolution spotlight SAR imaging," *IEEE Geosci. Remote Sens. Lett.*, vol. 11, no. 9, pp. 1460–1464, Sep. 2014.

[50] Y. Luo, F. Zhao, N. Li, and H. Zhang, "An autofocus Cartesian factorized backprojection algorithm for spotlight synthetic aperture radar imaging," *IEEE Geosci. Remote Sens. Lett.*, vol. 15, no. 8, pp. 1244–1248, Aug. 2018.

[51] Q. Dong, Z. Yang, G. Sun, and M. Xing, "Cartesian factorized back-projection algorithm for synthetic aperture radar," in *Proc. IEEE Int. Geosci. Remote Sens. Symp. (IGARSS)*, Jul. 2016, pp. 1074–1077.

[52] X. Chen, G.-C. Sun, M. Xing, B. Li, J. Yang, and Z. Bao, "Ground Cartesian back-projection algorithm for high squint diving Tops SAR imaging," *IEEE Trans. Geosci. Remote Sens.*, vol. 59, no. 7, pp. 5812–5827, Jul. 2021.

Yan Wang (Member, IEEE) received the B.S. degree in electronic information engineering and the Ph.D. degree in signal and information processing from the School of Information and Electronic Engineering, Beihang University, Beijing, China, in 2011 and 2016, respectively.

From 2016 to 2018, he was a Post-Doctoral Fellow with the Department of Electronic Engineering, Tsinghua University, Beijing. Since 2018, he has been an Assistant Professor with the School of Information and Electronics, Beijing Institute of Technology, Beijing; Beijing Institute of Technology Chongqing Innovation Center, Chongqing, China; and Yangtze Delta Region Academy, Jiaxing, China. His research interests include advanced synthetic aperture radar (SAR) imaging techniques, SAR interferometry, and SAR polarimetry techniques.

Xuan Wang (Graduate Student Member, IEEE) was born in Jilin, China, in 1997. He received the B.S. degree in electronic information engineering from the School of Information and Electronics, Beijing Institute of Technology, Beijing, China, in 2020. He is currently pursuing the Ph.D. degree with the Radar Research Laboratory, Beijing Institute of Technology.

His research interests mainly include spaceborne synthetic aperture radar terrain matching curved imaging technology and the design of SAR imaging algorithms for the spaceborne system.

Hanwei Sun (Member, IEEE) received the B.S. and Ph.D. degrees from Beijing Institute of Technology (BIT), Beijing, China, in 2007 and 2012, respectively.

From 2012 to 2014, he was a Post-Doctoral Researcher with the Department of Electronic Engineering, Tsinghua University, Beijing. He is currently a Senior Engineer with Beijing Institute of Radio Measurement, Beijing. His research interests include radar modeling and simulation, SAR imaging, and the design of SAR imaging algorithms for the airborne/spaceborne systems.

Ke Chen (Graduate Student Member, IEEE) received the B.S. degree in information countermeasure technology from the School of Electronic Engineering, Xidian University, Xi'an, China, in 2019. He is currently pursuing the Ph.D. degree with the School of Information and Electronics, Beijing Institute of Technology, Beijing, China.

His research interests include advanced synthetic aperture radar (SAR) imaging technology.

Qingjun Zhang (Member, IEEE) received the Ph.D. degree from Huazhong University of Science and Technology, Wuhan, China, in 2004.

He is currently a Professor of Satellite Engineering with China Academy of Space Technology, Beijing, China. He is also the Program Manager and the Chief Engineer of GF-3 and HY-2 Program, and the Chief Engineer of China–Brazil Earth Remote Sensing Satellite. He is also involved in the research of microwave remote sensing, especially in the synthetic aperture radar.

Dr. Zhang is a member of the Technical Committee of China Academy of Space Technology.

Qingrui Guo (Member, IEEE) was born in Hubei, China, in 2000. He received the B.S. degree in information countermeasure from Beijing Institute of Technology (BIT), Beijing, China, in 2022. He is currently pursuing the M.E. degree with the Radar Research Laboratory, BIT.

His research interests mainly include spaceborne synthetic aperture radar terrain matching curved imaging and system design.

Ziheng Liu (Graduate Student Member, IEEE) was born in Hubei, China, in 2000. He received the B.S. degree in electronic information engineering from Harbin Engineering University, Harbin, China, in 2022. He is currently pursuing the M.E. degree with the Radar Technology Research Institute, Beijing Institute of Technology, Beijing, China.

His research interests mainly include SAR system design and ambiguity suppression.

Yong Zhao received the B.S. degree from Beihang University (BUAA), Beijing, China, in 2021.

He is currently an Engineer with Beijing Institute of Radio Measurement, Beijing. His research interests mainly include the design of spaceborne synthetic aperture radar systems.

Heli Gao received the B.S. and Ph.D. degrees from the School of Electronic and Information Engineering, Beihang University, Beijing, China, in 2014 and 2020, respectively.

He is currently with the Institute of Remote Sensing Satellite, China Academy of Space Technology, Beijing. His research interests focus on the system design of satellite and SAR imaging processing.

Bingyi Li received the B.S. and Ph.D. degrees from Beijing Institute of Technology (BIT), Beijing, China, in 2013 and 2019, respectively.

He is currently a Senior Engineer with Beijing Institute of Radio Measurement, Beijing. His research interests include SAR imaging and the spaceborne SAR system design.

Dehua He received the B.S. degree in material science and engineering from Northwestern Polytechnical University, Xi'an, China, and the Ph.D. degree in aerospace science and technology from Beihang University, Beijing, China, in 2006 and 2011, respectively.

He is currently with the Institute of Remote Sensing Satellite, China Academy of Space Technology, Beijing. His research interests focus on the system design of satellite.

Guo Zhang (Member, IEEE) received the B.E. and Ph.D. degrees in photogrammetry and remote sensing from the School of Remote-Sensing and Information Engineering, Wuhan University, Wuhan, China, in 2000 and 2005, respectively.

His doctoral dissertation focuses on the rectification of high-resolution remote-sensing imaging in the absence of ground control points. Since 2005, he has been with the State Key Laboratory of Information Engineering in Surveying, Mapping, and Remote-Sensing (LIESMARS), Wuhan University, where he became a Professor in 2011. His research interests include space photogrammetry, geometric processing of spaceborne optical/SAR/InSAR imagery, altimetry, and high-accuracy image matching.

Zegang Ding (Senior Member, IEEE) received the B.S. and Ph.D. degrees in electronic engineering from Beijing Institute of Technology, Beijing, China, in 2003 and 2008, respectively.

He was a Visiting Scholar with the University of Birmingham, Birmingham, U.K., from January to June 2008, and Tohoku University, Sendai, Japan, from April to July 2016. Since July 2017, he has been a Full Professor with the School of Information and Electronics, Beijing Institute of Technology; Beijing Institute of Technology Chongqing Innovation Center, Chongqing, China; and Yangtze Delta Region Academy, Jiaxing, China. His research interests include synthetic aperture radar imaging and system design.

Tao Zeng (Senior Member, IEEE) received the B.S. and Ph.D. degrees from the Department of Electronic Engineering, Beijing Institute of Technology (BIT), Beijing, China, in 1994 and 1999, respectively.

In 1999, he joined BIT as a Teaching Staff, where he has been a Full Professor with the School of Information and Electronic since July 2005. Since 2019, he has been a Full Professor with Chongqing Innovation Center, Chongqing, China. His research interests include synthetic aperture radar imaging technology and real-time radar signal processing.